





## Article

# Characterisation of High Temperature Oxidation Phenomena during AISI 430 Stainless Steel Manufacturing under a Controlled H<sub>2</sub> Atmosphere for Bright Annealing

Irene Collado García <sup>1,2,\*</sup> , Andrés Núñez Galindo <sup>1</sup> , Juan F. Almagro Bello <sup>1</sup>, Juan M. González Leal <sup>3</sup>   
and Javier F. Botana Pedemonte <sup>2</sup> 

<sup>1</sup> Laboratory & Research Section, Technical Department, Acerinox Europa S.A.U., 11379 Palmones, Spain; andres.nunez@acerinox.com (A.N.G.); juan.almagro@acerinox.com (J.F.A.B.)

<sup>2</sup> Department of Materials Science, Metallurgical Engineering and Inorganic Chemistry, School of Engineering, University of Cadiz, 11519 Puerto Real, Spain; javier.botana@uca.es

<sup>3</sup> Department of Condensed Matter Physics, Faculty of Sciences, University of Cadiz, 11510 Puerto Real, Spain; juanmaria.gonzalez@uca.es

\* Correspondence: irene.collado@uca.es

**Abstract:** Localised-in-the-edge oxidation of four AISI 430 alloys was investigated after an industrial bright annealing process. The oxidised surface of each specimen was characterised by X-ray photoelectron spectroscopy (XPS), Raman-spectroscopy and SEM. The results showed that the selective oxidation of Cr and Mn took place at the coil edges of AISI 430. This led to the formation of an oxide scale based on Cr<sub>2</sub>O<sub>3</sub> and MnCr<sub>2</sub>O<sub>4</sub>. On the other hand, the formation of Cr(OH)<sub>3</sub> and MnOOH in the outer part of the oxide scale was related to the effect of the H<sub>2</sub>-N<sub>2</sub> environment on the annealing furnace. The results concluded that the composition of Cr and Mn in the alloy determined the composition of the oxidation products. However, the effect of annealing time was minor in this oxidation mechanism, which slightly contributed to an increase in the cation diffusion from the steel to the oxide. Finally, the results obtained indicate that the colouration of the coil edges displayed in each studied material varies according to the alloy chemical composition and annealing time.

**Keywords:** bright annealing; ferritic stainless steel; high temperature oxidation; SEM; Raman spectroscopy; XPS



**Citation:** García, I.C.; Galindo, A.N.; Bello, J.F.A.; Leal, J.M.G.; Pedemonte, J.F.B. Characterisation of High Temperature Oxidation Phenomena during AISI 430 Stainless Steel Manufacturing under a Controlled H<sub>2</sub> Atmosphere for Bright Annealing. *Metals* **2021**, *11*, 191. <https://doi.org/10.3390/met11020191>

Received: 15 December 2020

Accepted: 18 January 2021

Published: 21 January 2021

**Publisher's Note:** MDPI stays neutral with regard to jurisdictional claims in published maps and institutional affiliations.



**Copyright:** © 2021 by the authors. Licensee MDPI, Basel, Switzerland. This article is an open access article distributed under the terms and conditions of the Creative Commons Attribution (CC BY) license (<https://creativecommons.org/licenses/by/4.0/>).

## 1. Introduction

Stainless steel is known for its wide range of high-quality finish grades. Depending on customer requirements, the final annealing stage must ensure the proper surface finish and mechanical properties of stainless steel [1]. In order to reach a mirror finishing, bright annealing is performed as the final stage of the manufacturing route of stainless steel. During this stage, the material is exposed to a certain temperature followed by rapid cooling inside a reducing atmosphere furnace. A reducing gas mixture of dry 75% H<sub>2</sub>-25% N<sub>2</sub> is generally used by industry to protect stainless steel surfaces from becoming oxidised during annealing, which favours a mirror finishing. Nevertheless, flat AISI 430 stainless steel shows a coloration along both edges of the coil after bright annealing. This causes cost overrun in manufacturing, because it is necessary to remove the oxidised areas.

The localised coloration may be caused by several factors. One of them could be related to the fact that the coil goes through a washing and drying process before annealing. Afterwards, due to the distinctive cracks of AISI 430 generated during the previous rolling processes, the contaminants located within these cavities cannot be efficiently removed. Furthermore, after washing and drying, the relative humidity increases in these regions. According to literature [2–6], the presence of a minor amount of humidity within the annealing gas environment can favour the selective oxidation of alloying elements, such as Cr, Mn and Si. Under reducing environment, this localised oxidation is predominantly

controlled by the inward diffusion of oxygen through the oxide scale [7]. In industry, this oxidation phenomenon is characteristic of AISI 430 and does not take place in austenitic or duplex stainless steels. According to literature [8–10], the diffusivity of oxygen and alloying elements is more favoured in ferritic than in austenitic or duplex stainless steels.

Other authors have related the selective oxidation of alloying elements, under a certain atmosphere, with the partial pressure of the oxygen in the exposure environment, also known as dissociative pressure [7,11–15]. In other studies [6,9,16,17], the dew point (DP) has also been proposed as the main driving force for the selective oxidation of Cr and other minor alloying elements. However, in an industrial environment, none of the above-mentioned factors can be completely controlled.

Nonetheless, there are other factors that have not been studied in the literature to date, which could determine the features of the oxidation products formed during bright annealing. In the present work, the study of the influence of alloy composition and annealing time on the chemical nature of the oxidised surface is proposed. For this purpose, the environment composition of the oxidised surface was investigated using Raman and X-ray Photoelectron Spectroscopy. The morphology of the top oxide scale was studied using Focused Ion Beam Scanning Electron Microscopy (FIB-SEM). The results showed that the coloration was caused by the selective oxidation of Cr and Mn into  $\text{Cr}_2\text{O}_3$  and  $\text{MnCr}_2\text{O}_4$  during bright annealing, which was driven by a higher localised oxygen source at the edge surface of the studied AISI 430 coils. Furthermore, the concentration and phase proportion of  $\text{Cr}_2\text{O}_3$  and  $\text{MnCr}_2\text{O}_4$  on the oxidised surface depended merely on the alloy Cr and Mn concentrations, whereas the influence of the annealing time slightly increased the concentration of the oxidation products. This study aims to show that controlling the composition of AISI 430 ferritic stainless steel, according to the annealing conditions set for each steel, can contribute to minimising the effect of the oxidation process that takes place at the edges of the AISI 430 coils during bright annealing.

## 2. Materials and Methods

### 2.1. Materials and Bright Annealing Atmosphere

The AISI 430 ferritic stainless steel studied in this work was produced under conventional industrial conditions using an electric arc furnace, AOD converter and continuous casting. The reduction in slab thickness took place during hot rolling, and the material was recrystallised at the end of this stage using annealing treatment. After this, the final thickness of the coil was reached after the cold rolling stage. A final annealing process was performed in a reducing atmosphere in order to recrystallise the structure of the steel and, therefore, remove internal structural alterations produced during the rolling process. In addition, a bright or mirror finishing was achieved during this stage due to the  $\text{H}_2/\text{N}_2$  atmosphere of the annealing furnace. The gas of this furnace consists of 75%  $\text{H}_2$ – 25%  $\text{N}_2$  with 6.8 ppm of  $\text{O}_2$ . The control of the annealing environment is based on the dew point, which is equal to  $-40$  °C. The optimal conditions of bright annealing were set with respect to the oxidation/reduction equilibrium of Cr/ $\text{Cr}_2\text{O}_3$  of the passive film of stainless steel.

The selection of materials for this study was based on industrial needs. The oxidation located at the edges of the coils after the bright annealing process had a different appearance depending on the grade of AISI 430 ferritic stainless steel. In this way, a total of four samples with different annealing times were distinguished, where chromium and manganese varied from one specimen to the other. Table 1 shows the chemical composition of the four AISI 430 ferritic stainless steels studied in this paper. A430-2(A) and A430-2(B) show the lowest Cr concentration, whereas A430-1 and 3 have the highest composition of this element. On the other hand, the manganese concentration increases from the specimen A430-1 to A430-3. Cr and Mn concentrations are similar in A430-2(A) and A430-2(B).

**Table 1.** Chemical composition of A430-1, 2 and 3 alloys in mass percentage and exposure time during the heating stage of bright annealing.

| Material  | Fe (wt. %) | Si (wt. %)   | Mn (wt. %)   | Cr (wt. %)   | C (wt. %)      | N <sub>2</sub> (wt. %) | Annealing Time (s) |
|-----------|------------|--------------|--------------|--------------|----------------|------------------------|--------------------|
| A430-1    | Balance    | 0.42 ± 0.008 | 0.34 ± 0.008 | 17.0 ± 0.061 | 0.023 ± 0.0014 | 0.019 ± 0.0013         | 42                 |
| A430-2(A) | Balance    | 0.43 ± 0.007 | 0.52 ± 0.009 | 16.4 ± 0.060 | 0.027 ± 0.0014 | 0.023 ± 0.0014         | 42                 |
| A430-2(B) | Balance    | 0.48 ± 0.008 | 0.54 ± 0.009 | 16.4 ± 0.060 | 0.016 ± 0.0010 | 0.030 ± 0.0016         | 55                 |
| A430-3    | Balance    | 0.39 ± 0.007 | 0.78 ± 0.011 | 16.7 ± 0.061 | 0.030 ± 0.0015 | 0.030 ± 0.0016         | 50                 |

Additionally, Table 1 includes the annealing time for each sample. According to this information, the shortest annealing time was registered for the specimens A430-1 and A430-2(A), which were processed for 42 s. Moreover, A430-2(B) and A430-3 were annealed for 55 and 50 s, respectively.

## 2.2. Oxide Scale Characterisation

After the bright annealing process, samples were cut and metallographically prepared for oxide scale characterisation using the techniques described below. The nominal sample size for analysis methods was 15 × 15 mm. The plan view images of the samples were acquired by a Zeta Instruments Z-300 3D optical profilometer.

The X-ray photoelectron spectroscopy (XPS) technique offered both quantitative and qualitative information at a depth regime of 2–10 nm, and it offered a better understanding of the surface chemical environment of specimens studied after the bright annealing process. For this purpose, survey and high-resolution O 1s, Cr 2p, Fe 2p, Mn 2p, N 1s and Si 2p spectra were recorded. XPS measurements were carried out using a Kratos Axi Ultra DLD spectrometer equipped with an X-ray monochromatic source (50 W) and Al K $\alpha$  primary X-ray beam ( $h\nu = 1486.6$  eV). Spectral fitting was performed using CasaXPS version 2.3.18.

Raman spectroscopy allowed the assessment of the chemical nature of the oxides formed on the surface of the samples after the bright annealing process. A Jasco NRS-7200 Confocal Raman Microscope was used for this purpose, with a wavelength of the excitation laser of 532 nm, a wavenumber range of 8000–100 cm<sup>-1</sup> and a high-resolution CMOS camera for sample observation. The study was performed 100× by linear analyses of 201 points transversal to the rolling direction with a 50  $\mu$ m step size, and 10 mm of the surface was covered for this research. The reproducibility of the Raman spectroscopy and XPS techniques involved three analyses per sample. The XPS results showed the average of the three analyses, whereas the Raman results showed the most representative one of the three analyses.

Finally, the top view morphology of the samples was studied using the FIB-SEM Zeiss Crossbeam 550 equipped with an Oxford Instruments energy-dispersive X-ray spectrometer (EDS). Both secondary electron (SE) and energy selective backscattered (EsB) detectors were used for imaging.

## 3. Results

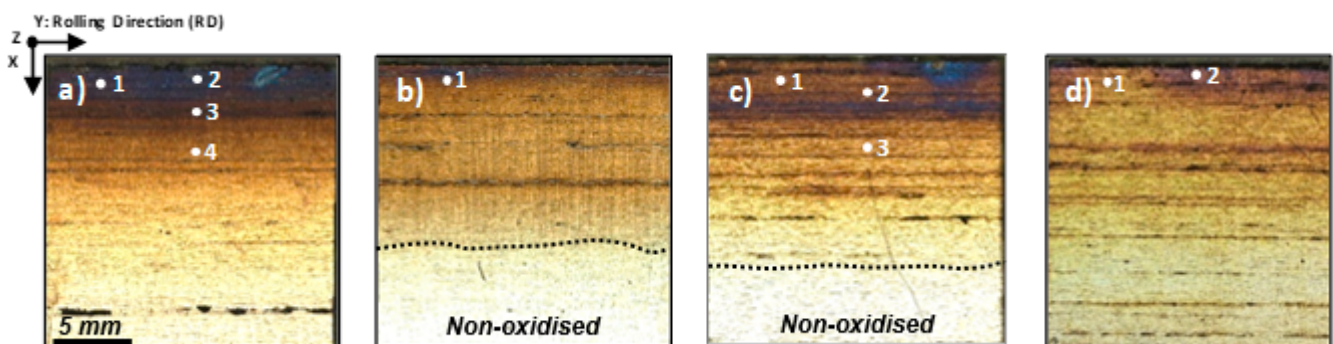
The characterisation of the selected materials in this paper was merely carried out on the surface. In this section, the results will be presented according to the method used for the surface characterisation.

Figure 1 shows the general view of the localised-in-the-edge oxidation of an AISI 430 ferritic stainless steel coil after bright annealing. This oxidation is characterised by presenting a colour degradation from the edge to middle sheet along the x-axis.



**Figure 1.** General view of the localised-in-the-edge oxidation of an AISI 430 ferritic stainless steel after bright annealing.

Figure 2 shows detailed plan view images obtained by using an optical profilometer of selected specimens after bright annealing. These specimens were acquired from the oxidised surface of the coil edge represented by the coloured area in Figure 1. The bright region that is clearly identified in Figure 2b,c corresponded to the non-oxidised surface of the steel. Figure 2a,c show a more intense blue colour by the edge, which changed gradually in the former and radically in the latter. However, a lower intensity of the colour by the edge could be seen in the specimens corresponding to Figure 2b,d compared to the other.



**Figure 2.** Plan view images obtained by optical profilometer of (a) A430-1, (b) A430-2(A), (c) A430-2(B) and (d) A430-3 specimens collected from coil edges after bright annealing.

Figure 2 points out that the appearance of the coloration is different for each of the samples. The following section presents the results obtained when characterising the oxidised areas shown in Figure 2, using different instrumental techniques.

### 3.1. X-ray Photoelectron Spectroscopy

In this work, XPS aims to analyse the composition of the top 5 nm of the oxidised surface and the oxidation states of the main elements. A430-1 and A430-3 were selected for this study. According to Table 1, A430-3 has higher %Mn and lower %Cr than A430-1, whereas the annealing time was longer in the former. Therefore, XPS allows us to study the influence of the alloy composition and annealing time on the surface composition of the oxidised areas after the bright annealing process.

Figure 3a,b show the survey XPS spectra obtained from the analysis of point “1”, represented in Figure 2a for A430-1 and for A430-3. These points of analysis were associated with the blue and yellow colours of the oxidised surface of A430-1 and A430-3, respectively.

In addition, Table 2 provides the average surface composition for each specimen in the area of analysis of Figure 2a,d.

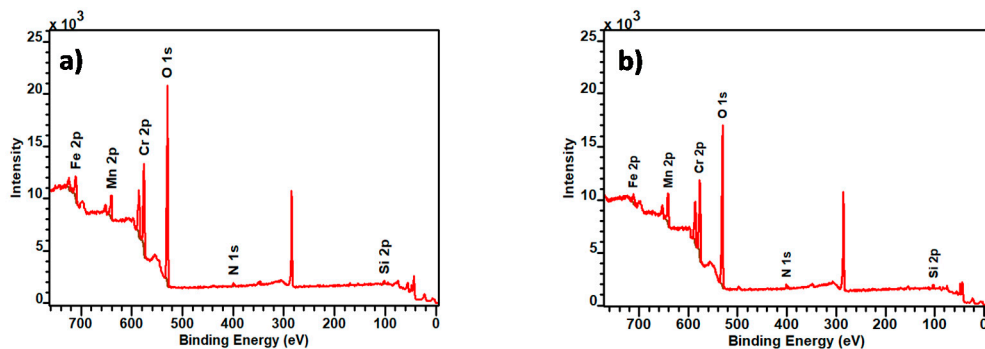


**Figure 3.** Survey X-ray photoelectron spectroscopy (XPS) spectra of (a) A430-1 and (b) A430-3 oxidation represented by point 1 in Figure 2a,d.

**Table 2.** Elemental surface analysis from survey spectra of Figure 2.

| Element | at. % A430-1 | at. % A430-3 |
|---------|--------------|--------------|
| O 1s    | 69.8 ± 0.639 | 71.6 ± 0.588 |
| N 1s    | 2.6 ± 0.331  | 2.4 ± 0.192  |
| Cr 2p   | 18.8 ± 0.291 | 16.0 ± 0.289 |
| Mn 2p   | 2.8 ± 0.153  | 4.5 ± 0.154  |
| Fe 2p   | 0.5 ± 0.123  | 0.4 ± 0.125  |
| Si 2p   | 5.5 ± 0.719  | 5.1 ± 0.661  |

According to Table 2, the composition of the oxide scale of these specimens consisted mainly of Cr, Mn and Si oxides. The results listed in Table 2 revealed that the main difference lays, principally, in Cr and Mn surface composition. It can be also observed that Cr content is higher in the oxidation products formed on the A430-1 surface, whereas Mn content is higher in A430-3.

The oxidation states of the four major elements on the oxidised surface of A430-1 and A430-3 samples were studied via high resolution XPS spectra. Figure 4 shows the spectra of the O 1s, Cr 2p, Mn 2p and Si 2p regions for both specimens.

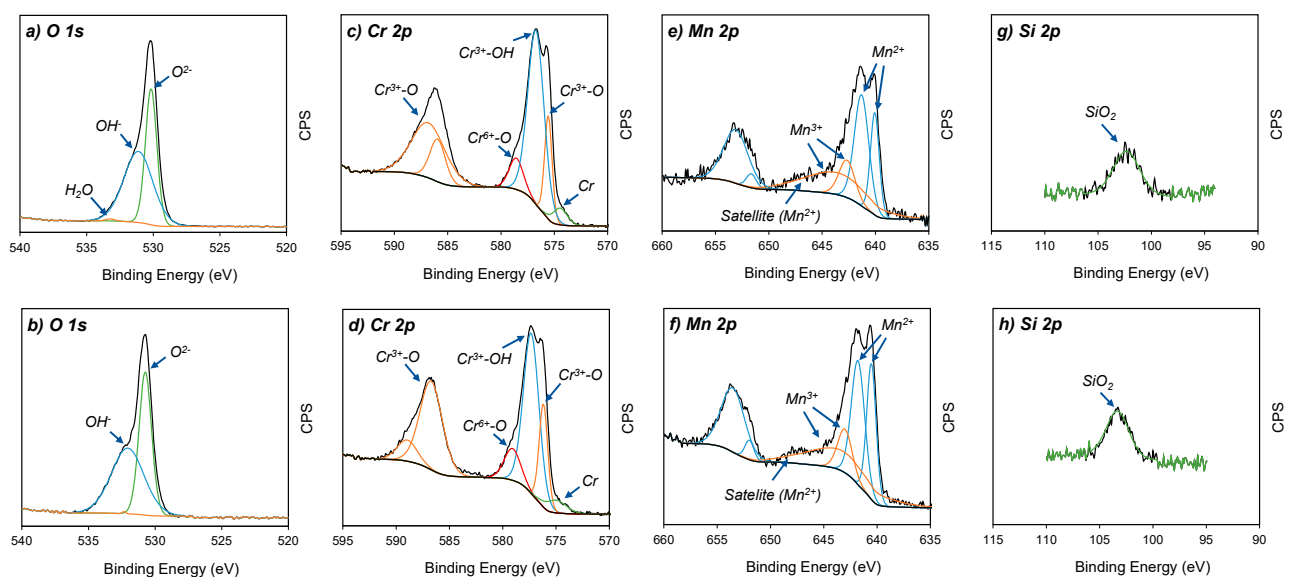


**Figure 4.** Core-level XPS spectra of (a,b) O 1s, (c,d) Cr 2p, (e,f) Mn 2p and (g,h) Si 2p from A430-1 and A430-3 oxide scales, respectively.

The relative proportion of each oxidation state acquired from the previous high resolution XPS spectra is listed in Table 3. The relative proportion of each oxidation state on the analysed oxide scale was calculated based on the peak area detected in Figure 4.

**Table 3.** The relative proportion of oxidation states identified in O 1s, Cr 2p, Mn 2p and Si 2p regions on the blue and yellow oxidised surface corresponding to A430-1 and A430-3, respectively.

| Oxidation State             | A430-1 (%) | A430-3 (%) |
|-----------------------------|------------|------------|
| O 1s                        |            |            |
| O <sup>2-</sup>             | 56.8       | 45.8       |
| OH <sup>-</sup>             | 42.7       | 54.2       |
| H <sub>2</sub> O            | 0.5        | -          |
| Cr 2p                       |            |            |
| Cr metal                    | 3.6        | 4.1        |
| Cr <sup>3+</sup> —oxide     | 48.2       | 49.9       |
| Cr <sup>3+</sup> —hydroxide | 41.7       | 38.1       |
| Cr <sup>6+</sup> —oxide     | 6.5        | 7.9        |
| Mn 2p                       |            |            |
| Mn <sup>2+</sup> —oxide     | 58.3       | 58.5       |
| Tetragonal site             | 18.2       | 24.4       |
| Octahedral site             | 40.1       | 34.1       |
| Mn <sup>3+</sup> —hydroxide | 41.7       | 41.5       |
| Si 2p                       |            |            |
| Si <sup>4+</sup> —oxide     | 100        | 100        |

Figure 4a,b show the O 1s spectra of the oxidised surface after the bright annealing process for both specimens. These spectra are composed of three peaks regarding O<sup>2-</sup> (530 eV), OH<sup>-</sup> (532 eV) and absorbed water (533 eV) [18]. According to Table 3, A430-1 reached a higher O<sup>2-</sup> relative concentration of 56.8%, compared to 42.7% of OH<sup>-</sup>. The opposite scenario was seen for A430-3, where O<sup>2-</sup> concentration was 45.8%, whereas OH<sup>-</sup> was 54.2%. In agreement with these results, the oxide scale formed on the oxidised surface of these samples after bright annealing is composed of both hydroxide and oxide components, where the oxide concentration was higher in the blue oxidised surface of A430-1 than in the yellow oxidised surface of A430-3.

The Cr 2p spectra in Figure 4c,d show four constituents, which are metallic Cr (574.2 eV), Cr<sub>2</sub>O<sub>3</sub> (575.7 eV), Cr(OH)<sub>3</sub> (577.3 eV) and CrO<sub>3</sub> (578.7 eV) [2,19]. The major component of these outer layers was Cr(OH)<sub>3</sub>. Table 3 reports that the relative ratio of Cr(OH)<sub>3</sub> was 67.3% and 64.9% for A430-1 and A430-3, respectively. On the other hand, the relative proportion of Cr<sub>2</sub>O<sub>3</sub> was slightly lower in A430-1 than A430-3.

According to the fitting lines of Mn 2p spectra in Figure 4e,f, four peaks centred at 640.1, 641.3, 642.7 and 643.6 eV were detected in the Mn 2p<sub>3/2</sub> region. Moreover, a satellite peak was found at 647.1 eV. In addition, the Mn 2p<sub>1/2</sub> region of each spectrum displayed two peaks, which were identified in 651.6 and 653.1 eV positions. The peaks centred at 640.1, 641.3, 651.6 and 653.1 eV were assigned to Mn<sup>2+</sup> ions [20]. The satellite feature identified in 647.1 eV is also a typical feature of Mn<sup>2+</sup> [21,22]. In agreement with Bao et al. [20], the Mn<sup>2+</sup> peak position was determined by oxide structures, where the BE 640.1 and 641.3 eV are attributed to the occupation of Mn<sup>2+</sup> ions in the tetragonal site and octahedral site, respectively. Mn<sup>2+</sup> ions of tetragonal sites are associated with MnCr<sub>2</sub>O<sub>4</sub> spinel structures [23], whereas octahedral sites are ascribed to the MnO structure [24].

On the other hand, the peaks identified at 642.7 and 643.6 eV corresponded to  $\text{Mn}^{3+}$  ions [25]. According to literature [26–28], these peaks are associated with the formation of  $\text{MnOOH}$ . In agreement with Table 3, the relative concentration of  $\text{Mn}^{2+}$  and  $\text{Mn}^{3+}$  oxidation states did not significantly differ between A430-1 and A430-3. However, the relative concentration of  $\text{MnCr}_2\text{O}_4$  was higher in A430-3 after a longer annealing time than A430-1.

Finally, Si 2p spectra are shown in Figure 4g,h. XPS analysis detected one peak at 133 eV. According to literature [29], this peak corresponds to  $\text{SiO}_2$ . According to the results shown in Table 3, the whole Si concentration measured by survey XPS in Table 2 corresponds to  $\text{SiO}_2$ . Therefore, the  $\text{SiO}_2$  concentration in the outer oxide layer was 5.5 at. % in sample A430-1 and 5.1 at. % in sample A430-3. The concentration of silicon on the surface was not influenced by alloy chemical composition nor the annealing time.

### 3.2. Raman Spectroscopy

The chemical nature of the products formed on the surface during the bright annealing process was studied using Raman spectroscopy. This technique has a penetration depth of around 90 nm, which is larger than XPS. Figure 5 shows a stack plot of the representative spectra of each material from areas where a more intense colour was observed. The point of analysis is represented by point 1 in all samples in Figure 2.

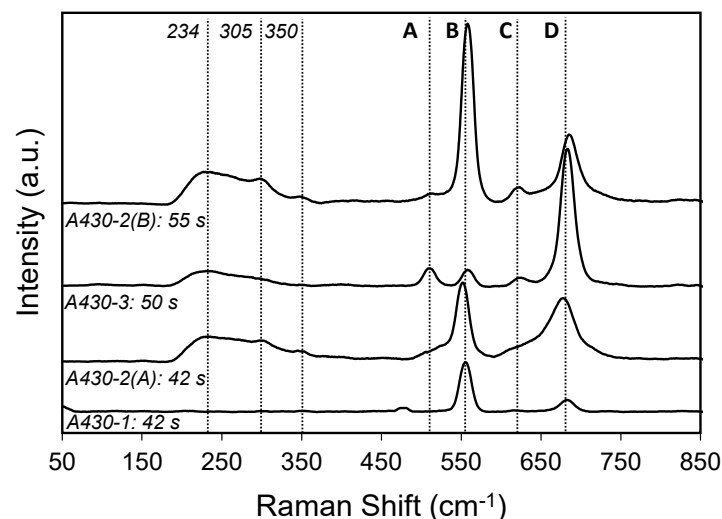


**Figure 5.** Raman spectra of point 1 from the samples shown in Figure 2a–d after bright annealing, exposed in the environment containing 75% $\text{H}_2$ –25% $\text{N}_2$ .

Four main peaks (A, B, C, D) are identified in these spectra, where the intensity of each band varies from one sample to the other. As it can be shown in Figure 5, the bands labelled as B, C and D are the main peaks of the oxide scale in all specimens. According to literature [30–32], peaks B and C at 555 and 618  $\text{cm}^{-1}$  correspond to the  $\text{Cr}_2\text{O}_3$  structure. The peak centred at 555  $\text{cm}^{-1}$  seemed to be asymmetric. This asymmetry could be due to the overlap of the  $\text{Cr}_2\text{O}_3$  peak with another peak associated with the presence of  $\text{MnOOH}$ . According to the literature [33], the main peak of  $\text{MnOOH}$  is identified at 558  $\text{cm}^{-1}$ . Moreover, the peaks A and D at 508 and 685  $\text{cm}^{-1}$  are attributable to  $\text{MnCr}_2\text{O}_4$  spinel [10,30]. Furthermore, a broad peak was found at 230  $\text{cm}^{-1}$ , which is associated with amorphous  $\text{Cr}_2\text{O}_3$  [32]. This band was identified in A430-2(A), A430-2(B) and A430-3 samples. A430-2(A) and A430-2(B) spectra displayed a weak peak centred at 305  $\text{cm}^{-1}$ , which corresponds to  $\text{Mn}_2\text{O}_3$  [33]. Finally, a weak band was observed at 350  $\text{cm}^{-1}$  in A430-2(A) and A430-2(B) spectra, and it is associated with Si oxides.

The analysis of the Raman spectra indicated that the oxide scale formed on the oxidised surface of the samples consisted mainly of  $\text{Cr}_2\text{O}_3$  and  $\text{MnCr}_2\text{O}_4$ . Figure 5 showed that  $\text{Cr}_2\text{O}_3$  was the major constituent of the oxidised surface of A430-1, A430-2(A) and A430-2(B) samples. On the other hand,  $\text{MnCr}_2\text{O}_4$  was the predominant oxide structure of the oxidised

surface of the A430-3 specimen. Compared to A430-1, the relative amount of  $\text{MnCr}_2\text{O}_4$  increased in A430-2(A) and A430-2(B) samples.

In addition, the relative concentration of the major oxides was studied by Raman along the x-axis of the oxidised surface of all the specimens, and the analysed surfaces in each sample are highlighted in Figure 2. This study aimed to relate the relative concentration of  $\text{Cr}_2\text{O}_3$  and  $\text{MnCr}_2\text{O}_4$  with the colour of the oxidised surface, which showed a change from the edge to the non-oxidised surface. Therefore, the intensities of  $\text{Cr}_2\text{O}_3$  and  $\text{MnCr}_2\text{O}_4$ , which correspond to peaks B and D in Figure 5, are plotted in Figure 6 as a function of the distance to the edge of sample A430-2(A).

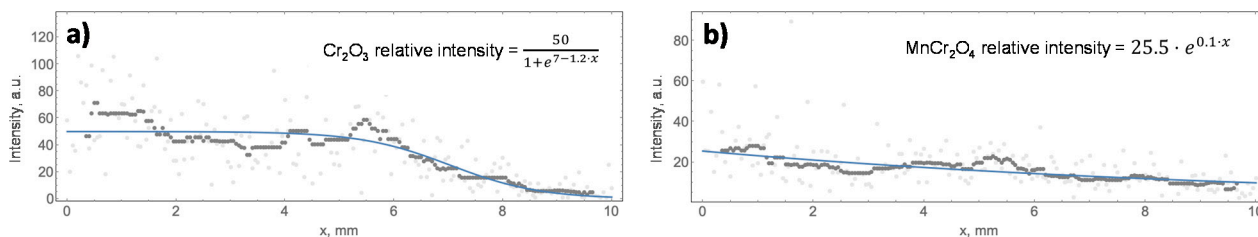


**Figure 6.** Linear Raman analysis of (a) peak B ( $\text{Cr}_2\text{O}_3$ ) and (b) peak D ( $\text{MnCr}_2\text{O}_4$ ) identified in Figure 5, measured along the x-axis of the A430-2(A) sample shown in Figure 2b, where sigmoid and exponential models were applied to fit the results, respectively.

The results from the Raman linear analysis of the four samples were fitted to two models. Equation (1) represents the sigmoid model used to characterise the evolution of the peak intensity displayed in Figure 6a. This model describes that the relative concentration of the oxide remains constant up to  $x_0$ , from which the concentration of the oxide begins to dramatically decrease. On the other hand, Equation (2) describes the evolution of the peak intensity when the results show an exponential curve plotted in Figure 6b. This model was related to a gradual decrease in the relative concentration of the oxide while the colour of the oxidised surface was changing from the edge and along the x-axis.

$$y = a / (1 + \exp(x_0 - bx)), \quad (1)$$

$$y = n \cdot \exp(mx), \quad (2)$$

In Equations (1) and (2), “a” and “n” are the maximum intensity of the corresponding peak and represent the maximum concentration of  $\text{Cr}_2\text{O}_3$  and  $\text{MnCr}_2\text{O}_4$  in the analysed areas. On the other hand, in Equation (1), “ $x_0$ ” represents the position of the peak intensity-drop, while “b” is the slope of the sigmoid curve after  $x_0$ . Finally, “m” represents the slope of the exponential curve of Equation (2) and gives information about the variation of the oxide concentration on the studied surface area. The parameters of each curve fitting of the results of the linear Raman analysis, as shown in Figure 6, are included in Tables 4 and 5.

**Table 4.** Parameters *a*, *n* (sigmoid/exponential maximum intensity of the peak), *b*, *m* (sigmoid/exponential curve spread) and  $x_0$  (sigmoid function) set for  $550 \text{ cm}^{-1}$  Raman shift models, which correspond to  $\text{Cr}_2\text{O}_3$  provided by the linear Raman analysis of AISI 430 samples.

| Sample    | Annealing Time (s) | $\text{Cr}_2\text{O}_3$ |                 |            |                 |                 | Model        |
|-----------|--------------------|-------------------------|-----------------|------------|-----------------|-----------------|--------------|
|           |                    | <i>a</i> (a.u.)         | <i>b</i> (a.u.) | $x_0$ (mm) | <i>n</i> (a.u.) | <i>m</i> (a.u.) |              |
| A430-1    | 42                 | -                       | -               | -          | 139.0           | 0.38            | Equation (2) |
| A430-2(A) | 42                 | 50.0                    | 1.22            | 7.0        | -               | -               | Equation (1) |
| A430-2(B) | 55                 | 89.0                    | 0.55            | 6.0        | -               | -               | Equation (1) |
| A430-3    | 50                 | -                       | -               | -          | 6.0             | 0.01            | Equation (2) |



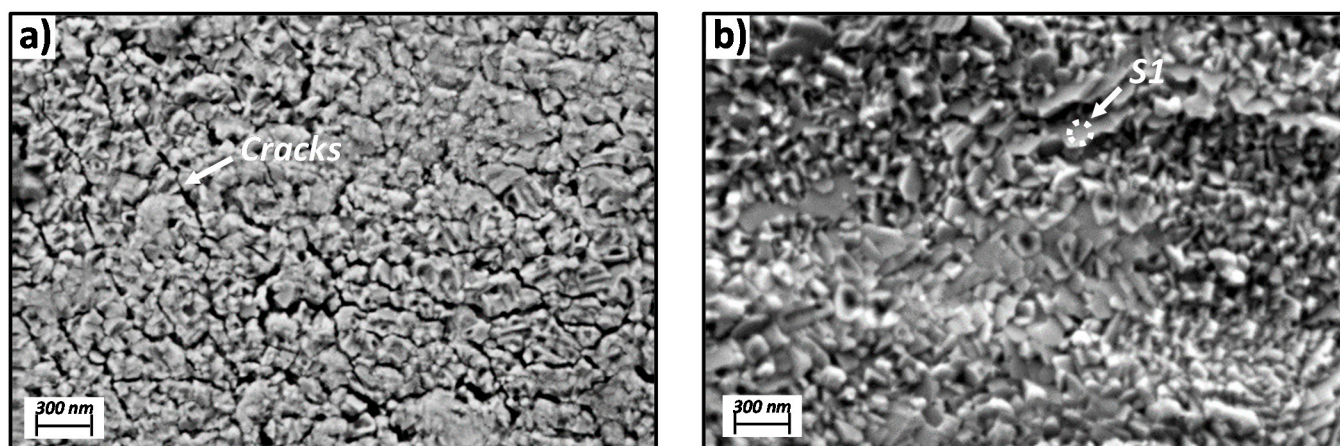
**Table 5.** Parameters  $a$ ,  $n$  (sigmoid/exponential maximum intensity of the peak),  $b$ ,  $m$  (sigmoid/exponential curve spread) and  $x_0$  (sigmoid function) set for  $680\text{ cm}^{-1}$  Raman shift models, which correspond to the  $\text{MnCr}_2\text{O}_4$  provided by the linear Raman analysis of AISI 430 samples.

| Sample    | Annealing Time (s) | $\text{MnCr}_2\text{O}_4$ |            |            |            |            | Model        |
|-----------|--------------------|---------------------------|------------|------------|------------|------------|--------------|
|           |                    | $a$ (a.u.)                | $b$ (a.u.) | $x_0$ (mm) | $n$ (a.u.) | $m$ (a.u.) |              |
| A430-1    | 42                 | -                         | -          | -          | 43.1       | 0.16       | Equation (2) |
| A430-2(A) | 42                 | -                         | -          | -          | 25.5       | 0.10       | Equation (2) |
| A430-2(B) | 55                 | 47.3                      | 0.46       | 7.0        | -          | -          | Equation (1) |
| A430-3    | 50                 | -                         | -          | -          | 119.0      | 0.13       | Equation (2) |

### 3.3. SEM Morphology

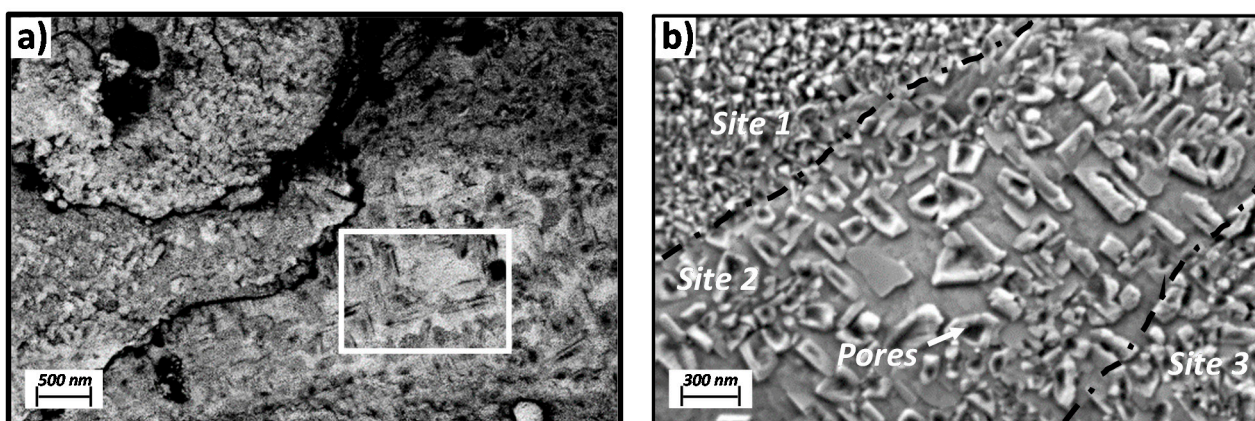
SEM imaging was carried out to study the morphology of the top oxides formed on the oxidised surface during the bright annealing process. The points of study are displayed in Figure 2.

Figure 7a,b show SEM plan view images of points 2 and 3, respectively, from Figure 2a, which corresponds to the A430-1 specimen. These points represent blue and the border between the blue and yellow oxidation colours, respectively. The morphology associated with the blue oxidised surface in Figure 7a was uniform with no defined oxide crystals, which encouraged the formation of cracks. On the other hand, heterogeneous morphology based on fine oxide crystals can be identified in the blue–yellow oxidised area of Figure 7b. In this image, some larger oxide crystals, labelled as S1, could be detected.



**Figure 7.** SEM/SE plan views (EHT: 2.00 keV) of (a) point 2 and (b) point 3 of A430-1 oxide scale after bright annealing shown in Figure 2a.

Figure 8a,b show SEM images of point 4 in Figure 2a, which corresponds to the yellow oxidised surface of A430-1. Figure 8b provides a higher magnification image acquired in the area shown in Figure 8a. The latter image was acquired by an EsB detector in order to study compositional changes in this region associated with changes in brightness. Figure 8b suggests that the morphology of the yellow area was based on fine oxide crystals, with an average diameter of less than 50 nm, as can be observed in Sites 1 and 3. However, some faceted oxide structures were widely distributed over the yellow oxidised surface, which showed a different morphology; see Site 2. This site consisted of a smaller number of oxide crystals, which were larger in size. These structures had grown mostly around pores.



**Figure 8.** (a) SEM/BSE (EHT: 1.50 keV) and (b) SEM/SE (EHT: 2.00 keV) plan view of point 4 of A430-1 oxide scale after bright annealing shown in Figure 2a.

Furthermore, the lowest part of the faceted oxide structures of Figure 8b showed a smooth morphology where the larger oxide structures started growing. This smooth morphology is represented in Figure 8a by the brighter area, which provides supporting evidence for the change in composition in Site 2 compared to the surrounding areas in Site 1 and 3.

The morphology of the oxidised surface is also evaluated for A430-2(B) in Figure 9a,b and A430-3 in Figure 9c,d. The studied areas are represented by points 2 and 3 in Figure 2c and point 2 in Figure 2d, respectively, for each specimen.

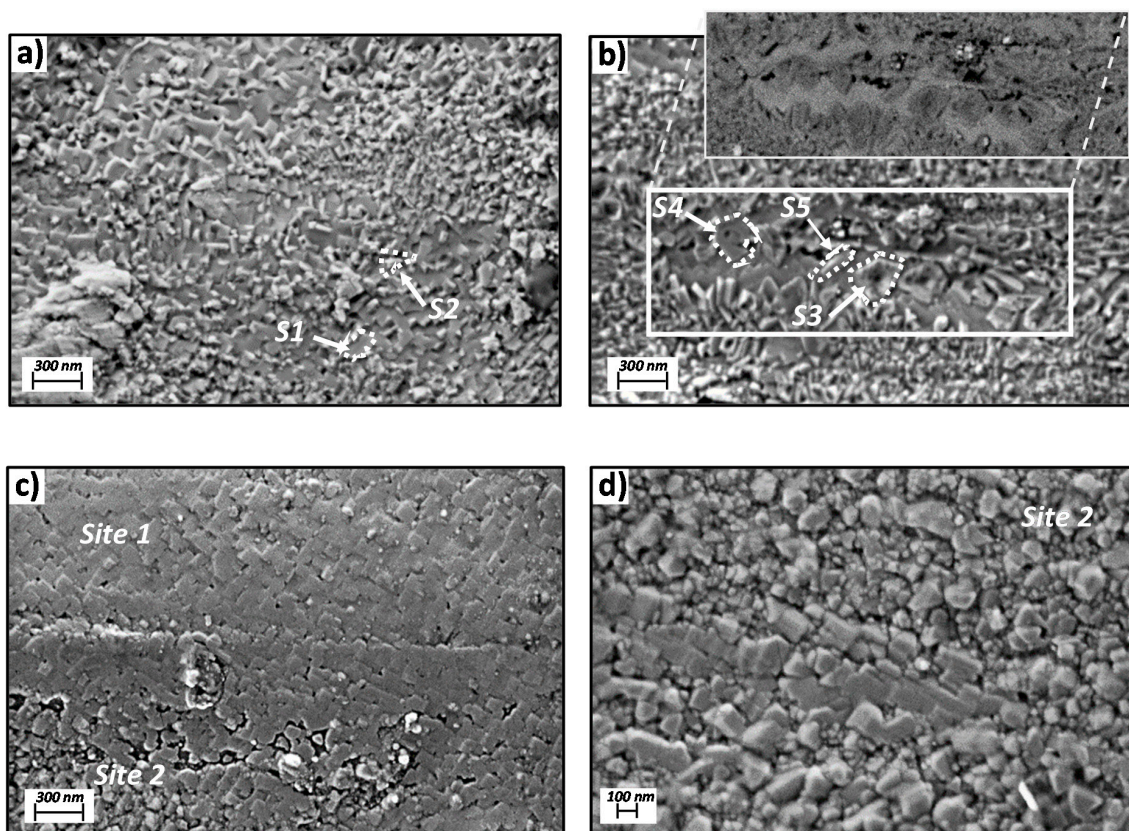


**Figure 9.** (a) SEM/SE plan view (EHT: 2.00 keV) of point 2 and (b) SEM/SE and zoomed-in SEM/BSE plan view of point 3 of A430-2(B) oxide scale after bright annealing shown in Figure 2c; SEM/InLens plan view (EHT: 1.50 keV) of (c) point 2 and (d) Site 2 zoomed-in image of A430-3 oxide scale after bright annealing shown in Figure 2d.

Compared to A430-1, better-defined and smaller oxide structures can be observed on these two samples regardless of the colour of the studied surface. Concerning A430-2(B) in Figure 9a, flat cubic structures were identified in S1, whereas smaller oxide grains were found in S2. Additionally, some pores were widely dispersed over the surface. According to Figure 9b, faceted oxide structures were found, where larger and irregular oxide crystals had grown within this region; see S3–S5. Furthermore, this area showed the smooth morphology previously identified in Figure 9b. The SEM/BSE image in Figure 9b gave evidence that the change of morphology in this area, where faceted oxide structures were found, was related to a change in composition.

Finally, Figure 9c showed that A430-3 formed larger and well-defined top-oxide crystals, whereas the oxide layer was uniform in Site 1. This site was covered by flat cubic structures forming a homogeneous layer. Figure 9d shows that Site 2 was based on irregular oxide structures, which gave the surface a rougher appearance. Surface analysis of this specimen as well as for A430-1 was carried out by XPS.

#### 4. Discussion

XPS and Raman spectroscopy were used to characterise the chemical properties of the oxide scale formed on the oxidised surface of the specimens shown in Figure 2, which were acquired from the coil edges of AISI 430 stainless steel after the bright annealing process. Raman spectroscopy analyses the oxidised surface composition at 100 nm thick, whereas XPS has a lower penetration depth of 5 nm, which allows us to analyse the outer layer of this surface. According to the XPS spectra in Figure 3, chromium and manganese are the major metal elements which compose the oxidised surface of A430-1 and A430-3 samples. At the same time, the data listed in Table 2 show that the relative concentration of Cr and Mn calculated from Figure 3 is 18.8% and 2.8% in sample A430-1 and 16.0% and 4.5% in sample A430-3, respectively. The concentration of these elements was higher on the oxidised surface than in the bulk. This is due to the fact that the outward migration of Cr and Mn during oxidation produces an ascending steel-surface concentration gradient.

On the other hand, Raman spectra of Figure 5 demonstrate that the oxidised surface of the four specimens after the bright annealing process is mainly composed of  $\text{Cr}_2\text{O}_3$  and  $\text{MnCr}_2\text{O}_4$ . Thus, it is possible to support that the colouration observed in the samples of Figure 2 takes place due to the localised selective oxidation of Cr and Mn at the surface of the coil edges of AISI 430 during the bright annealing process. According to Figure 5, the intensity of the  $\text{Cr}_2\text{O}_3$  band is significantly larger than that of  $\text{MnCr}_2\text{O}_4$  on the oxidised surface of A430-1, A430-2(A) and A430-2(B) samples. However, the Raman spectrum of the A430-3 sample showed that the intensity of the  $\text{MnCr}_2\text{O}_4$  band is higher than that assigned to  $\text{Cr}_2\text{O}_3$ .

Raman linear analysis allows us to identify that the effect of alloy composition on the oxidation phenomenon is higher than that of annealing time. Generally, the influence of alloy composition is mainly determined by the Cr and Mn loading in the steel. The effect of alloying Cr content can be identified in Table 4, comparing the maximum intensity of the  $\text{Cr}_2\text{O}_3$  band of A430-1 and A430-2(A) samples. Thus, it is observed that decreasing the alloying Cr loading from 17.0% (A430-1) to 16.4% (A430-2(A)) after 42 s of annealing decreases the maximum relative intensity of the  $\text{Cr}_2\text{O}_3$  band from 139 to 50, respectively.

On the other hand, the effect of Mn content in the alloy can be observed in Table 5, concerning the linear Raman analysis of the  $\text{MnCr}_2\text{O}_4$  band. The data included in Table 5 show that the increase in alloying Mn loading in sample A430-3 leads to an increase in the maximum relative intensity of the  $\text{MnCr}_2\text{O}_4$  band to 119. The value of this parameter is significantly lower in the other specimens. Moreover, the intensity of the  $\text{Cr}_2\text{O}_3$  band in sample A430-3 dramatically decreases to six, indicating the  $\text{Cr}_2\text{O}_3$  formation is slowed down when increasing manganese concentration in the alloy. This is also observed in XPS data included in Table 2. According to these results, by increasing the Mn content in the alloy from 0.34% (A430-1) to 0.78% (A430-3), the Mn surface composition increases from 2.8% to 4.5%, whereas the surface Cr composition decreases from 18.8% to 16.0%.

Finally, regarding annealing time, A430-2(A) and A430-2(B) Raman spectra of Figure 5 indicate that the relative intensity of  $\text{Cr}_2\text{O}_3$  and  $\text{MnCr}_2\text{O}_4$  peaks significantly increases with increasing annealing time from 42 to 55 s for similar alloy composition. According to Tables 4 and 5, the maximum intensity of  $\text{Cr}_2\text{O}_3$  and  $\text{MnCr}_2\text{O}_4$  bands is 50.0 and 25.5 in the A430-2(A) specimen, respectively. It can be observed that when increasing the annealing time in sample A430-2(B), the intensity of these bands increases to 89.0 and 47.3, respectively. Therefore, it can be concluded that annealing time slightly contributes to increasing the selective oxidation of Cr and Mn, although the alloy composition drives the whole oxidation mechanism, as previously discussed.

On the other hand, high resolution XPS analysis of the O 1s region in Figure 4a,b reveals that there is an increment in hydroxide species in the outer part of the oxide scale. The presence of hydroxides can be associated with the reaction of metal elements with water vapour under the  $\text{H}_2$ -controlled atmosphere of the annealing furnace [19]. According to the data included in Table 3, increasing annealing time from 42 s in sample A430-1 to 50 s in sample A430-3 leads to an increase in the metal hydroxide concentration from 42.7% to 54.2% in the outer part of the oxide scale of the samples, respectively.

The analysis of the Cr 2p and Mn 2p regions shown in Figure 4c–f indicates that  $\text{Cr}(\text{OH})_3$  and  $\text{MnOOH}$  are the major constituents of the outer surface scale formed during the bright annealing process. The results obtained indicate that  $\text{Cr}(\text{OH})_3$  is the predominant product. In addition, the Cr 2p region displayed in Figure 4c,d determines that Cr forms  $\text{Cr}^{3+}$  oxide and hydroxide. Moreover,  $\text{Cr}^{6+}$  was identified as  $\text{CrO}_3$ . In agreement with Table 3, the relative composition of  $\text{CrO}_3$  slightly increased from 6.5% to 7.9% when increasing annealing time from 42 to 50 s. Furthermore, Table 3 shows that  $\text{Cr}(\text{OH})_3$  decreases from 41.7 to 38.1% when increasing annealing time. Overall,  $\text{CrO}_3$  and  $\text{Cr}(\text{OH})_3$  exist in the intermediate responsible for the evaporation of chromium [34,35], where increasing annealing time favours the oxidation of  $\text{Cr}_2\text{O}_3$  into  $\text{CrO}_3$ .

On the other hand, XPS spectra of Mn 2p region shown in Figure 4e,f reported that manganese can be found in the form of  $\text{Mn}^{2+}$  and  $\text{Mn}^{3+}$ . According to Table 3, the relative concentration of  $\text{Mn}^{2+}$  and  $\text{Mn}^{3+}$  in the outer part of the oxide scale is 58.3% and 41.7% in sample A430-1 and 58.5% and 41.5% in sample A430-3. These results indicate that the concentration of the different Mn species does not vary, significantly, when increasing annealing time. Having analysed the position of the peaks that appear in the spectra included in Figure 4e,f, the presence of MnO and  $\text{MnCr}_2\text{O}_4$  was identified [20]. The data listed in Table 3 allow us to conclude that, when increasing annealing time, the proportion of  $\text{MnCr}_2\text{O}_4$  increases from 18.2% in sample A430-1 to 24.4% in sample A430-3. In addition, these results indicate that MnO is the main  $\text{Mn}^{2+}$  product, with a proportion of 40.1% in sample A430-1 and 34.1% in sample A430-3.

The results obtained by XPS and Raman were also used to identify the origin of the different colours on the edge of the coils after bright annealing. Raman linear analysis in Figure 6 shows that the intensities of  $\text{Cr}_2\text{O}_3$  and  $\text{MnCr}_2\text{O}_4$  bands are higher by the edge and decrease along the x-axis toward the non-oxidised surface. Therefore, it can be concluded that the colour of the oxidised surface changes as the relative concentration of  $\text{Cr}_2\text{O}_3$  and  $\text{MnCr}_2\text{O}_4$  decreases from the edge to the middle of the coil.

Comparing Figure 2a,d, which correspond to A430-1 and A430-3 samples, it can be observed that the former showed a blue colour by the edge, which was not displayed by sample A430-3. According to Table 4, the maximum relative intensity of the  $\text{Cr}_2\text{O}_3$  band is 139 in sample A430-1 and six in sample A430-3. On the other hand, the maximum relative intensities of the  $\text{MnCr}_2\text{O}_4$  band, listed in Table 5, are 43.1 and 119, respectively. Therefore, it is concluded that the blue colour of the oxidised surface of AISI 430 after the bright annealing process is directly related to the higher concentration of  $\text{Cr}_2\text{O}_3$ . According to Young et al. [4], alloying Cr concentrations above 16% may drive an overgrowth of  $\text{Cr}_2\text{O}_3$  due to an increase in the Cr reservoir in the alloy/oxide interface [36] prompted by high temperatures of around 900 °C.

Moreover, the SEM plan view study reveals that different morphologies can be identified between the blue and yellow sites of the oxidised surface. Thus, sample A430-1 shows in Figure 7a a more homogeneous and compact oxide layer in the blue area. Some cracks can be identified in this region, which are associated with residual stress removal [37]. On the other hand, according to Figures 7b and 8b, the yellow area presents a heterogeneous morphology due to the diversity in size of the oxide crystals, where the structures of the oxides are well defined, unlike the previous blue area. There are many large oxide grains and voids, which contribute to increasing the level of defects in the oxide layer.

In contrast, considering SEM images corresponding to sample A430-2(B) in Figure 9a, it is observed that oxides of smaller size are formed, with better defined structures and greater crystallinity than those that appear in Figure 7a for sample A430-1. In addition, SEM images in Figure 9b show that the morphology of the top oxide scale is similar at different points of sample A430-2(B) from the edge of the oxidised surface, unlike in sample A430-1.

Finally, the role of manganese on the top oxide morphology was also analysed by the SEM plan view study in Figure 9c,d. It must be taken into consideration that the alloying Mn content is 0.34 wt.% in sample A430-1 and 0.78 wt.% in sample A430-3, while the Cr content is similar in both samples. The analysis of Figure 9c,d reports that the increase in the alloying Mn content leads to the formation of well-defined and larger oxide particles. Therefore, it is concluded that the predominant content of  $\text{MnCr}_2\text{O}_4$  compared to  $\text{Cr}_2\text{O}_3$  promotes the formation of a dense, highly crystalline and pore-free layer of oxide that prevents the development of the blue coloration at the edge of the coils after the bright annealing process.

## 5. Conclusions

In this work, oxidised samples of different ferritic stainless steel grades with bright finish were characterised. The specimens were obtained under industrial conditions from the edge of ferritic stainless steel coils selected for this study, after a bright annealing process, which took place in a vertical furnace containing a reducing atmosphere based on  $\text{H}_2/\text{N}_2$ . The influence of the chemical composition of ferritic stainless steels and the annealing time on the oxidation phenomenon that takes place at the edges of the coils was studied.

The results obtained from the analysis by XPS, Raman spectroscopy and SEM allow us to conclude that a selective oxidation of Cr and Mn takes place at the coil edges of the studied AISI 430 ferritic stainless steel during bright annealing. As a result, the oxide scale formed is mainly based on  $\text{Cr}_2\text{O}_3$  and  $\text{MnCr}_2\text{O}_4$ . The characterisation by means of XPS and Raman spectroscopy revealed that the effect of alloying Cr and Mn composition is slightly higher than that of annealing time on the localised selective oxidation.

The XPS results show that  $\text{Cr}(\text{OH})_3$  and  $\text{MnOOH}$  are formed on the outer part of the oxide layer as a result of the interaction of metallic Cr and Mn with the water present in the cracks of the edges of ferritic stainless steel coils. A slight decrease in the content of Cr in the alloy from 17 to 16.7 wt. % led to a decrease in the outer surface Cr concentration from 18.8 to 16 at. %. Furthermore, as the Mn content of the alloy increased from 0.34 to 0.78 wt. %, the concentration of  $\text{MnCr}_2\text{O}_4$  in this outer part of the surface increased from 0.51 to 1.09 at. %. On the other hand, as the annealing time increased from 42 to 50 s, the relative proportion of  $\text{CrO}_3$  slightly increased from 6.5 to 7.9%. This was due to the fact that the oxidation of  $\text{Cr}_2\text{O}_3$  into  $\text{CrO}_3$  took place for a longer duration in this outer part of the oxide layer after 50 s of exposure.

In addition, the results obtained from the linear Raman analysis and SEM make it possible to establish that the colour of the oxidised surface at the edges of ferritic stainless steel coils is related to the concentration of  $\text{Cr}_2\text{O}_3$  and  $\text{MnCr}_2\text{O}_4$ . The intensity of this colour changes in all the specimens as the relative concentration of  $\text{Cr}_2\text{O}_3$  and  $\text{MnCr}_2\text{O}_4$  decreases exponentially or sigmoidal from the edge to the middle of the coils. As the concentration of  $\text{Cr}_2\text{O}_3$  and  $\text{MnCr}_2\text{O}_4$  decreases, the morphology of the top-oxide layer varies, and the density of the oxide layer decreases. In sample A430-1, the blue colour predominates in the

area with the highest concentration of  $\text{Cr}_2\text{O}_3$ , associated with a maximum Raman intensity of 139. Therefore, this colour is associated with an overconcentration of  $\text{Cr}_2\text{O}_3$  due to a higher alloying Cr concentration of 17 wt. % and lower alloying Mn concentration of 0.34 wt. % compared to the other specimens. On the other hand, in sample A430-3, the yellow colour is the predominant colour on the oxidised surface. The higher alloying Mn composition of 0.78 wt. % and longer annealing time of 50 s of this sample caused the higher formation of  $\text{MnCr}_2\text{O}_4$  on the oxidised surface of this specimen, corresponding to a maximum Raman intensity of 119. Therefore, most of the Cr of the oxide scale became part of the octahedral site of the spinel structure of  $\text{MnCr}_2\text{O}_4$ , which led to a decrease in the  $\text{Cr}_2\text{O}_3$  concentration of the oxidized surface, which corresponded to a maximum Raman intensity of six.

Overall, the conclusions that arise from the characterisation carried out in this paper allow us to reduce the oxidation of the edges of the ferritic stainless steel coils during the bright annealing process. It is desirable to work with alloys that contain chromium concentrations around 16.5 wt. %, and to keep the manganese concentration between 0.5 and 0.8 wt. %. Therefore, the blue colour will be prevented in all cases, whereas the maximum distance from the edge of the coil reached by the oxidation will decrease. Finally, additional studies will be carried out in the future under controlled exposure conditions. This aims to achieve a better understanding of the influences of parameters involved in industrial bright annealing processes, such as dew point, on the behaviour of the different AISI 430 steel grades against oxidation. Simultaneously, oxidised samples will be studied by means of transmission electron microscopy in order to improve the cross-section characterisation method of the oxidation products formed during exposure.

**Author Contributions:** I.C.G.: Conceptualization, Investigation and Writing—original draft preparation. A.N.G.: Methodology, Resources and Formal Analysis. J.M.G.L.: Formal Analysis and Software. J.F.A.B.: Supervision, Validation and Funding acquisition. J.F.B.P.: Supervision and Writing—Reviewing and Editing. All authors have read and agreed to the published version of the manuscript.

**Funding:** This research was funded by the “Proyectos de I+D Individuales” programme, Centro para el Desarrollo Tecnológico Industrial (CDTI), Ministerio de Economía y Competitividad from the Spanish Government—project “FERRINOP”.

**Conflicts of Interest:** The authors declare no conflict of interest. The funders had no role in the design of the study; in the collection, analyses, or interpretation of data; in the writing of the manuscript, or in the decision to publish the results.

## References

1. Acerinox, S.A. Cedinox Spanish Stainless Steel Investigation & Research Association, (n.d.). Available online: <https://www.cedinox.es> (accessed on 20 April 2020).
2. Swaminathan, S.; Spiegel, M. Effect of alloy composition on the selective oxidation of ternary Fe-Si-Cr, Fe-Mn-Cr model alloys. *Surf. Interface Anal.* **2008**, *40*, 268–272. [[CrossRef](#)]
3. Hashimoto, K.; Asami, K.; Kawashima, A.; Habazaki, H.; Akiyama, E. The role of corrosion-resistant alloying elements in passivity. *Corros. Sci.* **2007**, *49*, 42–52. [[CrossRef](#)]
4. Young, D.J.; Zurek, J.; Singheiser, L.; Quadackers, W.J. Temperature dependence of oxide scale formation on high-Cr ferritic steels in Ar-H<sub>2</sub>-H<sub>2</sub>O. *Corros. Sci.* **2011**, *53*, 2131–2141. [[CrossRef](#)]
5. Yu, Y.; Shironita, S.; Souma, K.; Umeda, M. Effect of chromium content on the corrosion resistance of ferritic stainless steels in sulfuric acid solution. *Heliyon* **2018**, *4*, e00958. [[CrossRef](#)] [[PubMed](#)]
6. Kim, Y.; Lee, J.; Shin, K.S.; Jeon, S.H.; Chin, K.G. Effect of dew point on the formation of surface oxides of twinning-induced plasticity steel. *Mater. Charact.* **2014**, *89*, 138–145. [[CrossRef](#)]
7. Schütze, M.; Rensch, D.; Schorr, M. Parameters determining the breakaway oxidation behaviour of ferritic martensitic 9%Cr steels in environments containing H<sub>2</sub>O. *Corros. Eng. Sci. Technol.* **2004**, *39*, 157–166. [[CrossRef](#)]
8. Cvijović, I.; Parezanović, I.; Spiegel, M. Influence of H<sub>2</sub>-N<sub>2</sub> atmosphere composition and annealing duration on the selective surface oxidation of low-carbon steels. *Corros. Sci.* **2006**, *48*, 980–993. [[CrossRef](#)]
9. Norden, M.; Blumenau, M.; Wuttke, T.; Peters, K.J. The change of steel surface chemistry regarding oxygen partial pressure and dew point. *Appl. Surf. Sci.* **2013**, *271*, 19–31. [[CrossRef](#)]
10. Young, D.J. *High Temperature Oxidation and Corrosion of Metals*, 2nd ed.; Elsevier: Sydney, Australia, 2008; ISBN 9780081001011.

11. Ehlers, J.; Young, D.J.; Smaardijk, E.J.; Tyagi, A.K.; Penkalla, H.J.; Singheiser, L.; Quadackers, W.J. Enhanced oxidation of the 9%Cr steel P91 in water vapour containing environments. *Corros. Sci.* **2006**, *48*, 3428–3454. [CrossRef]
12. Yin, H.; Yuen, W.Y.D.; Young, D.J. Effects of water vapour and oxygen partial pressures on low carbon steel oxidation in N<sub>2</sub>-H<sub>2</sub>-H<sub>2</sub>O mixtures. *Mater. Corros.* **2012**, *63*, 869–877. [CrossRef]
13. Nickel, H.; Wouters, Y.; Thiele, M.; Quadackers, W.J. The effect of water vapor on the oxidation behaviour of 9%Cr steels in simulated combustion gases. *Am. Soc. Mech. Eng. Press. Vessel. Pip. Div. PVP* **1997**, *359*, 269–273.
14. Tanahashi, M.; Furuta, N.; Yamauchi, C.; Fujisawa, T. Phase equilibria of the MnO-SiO<sub>2</sub>-CrOx system at 1873 K under controlled oxygen partial pressure. *ISIJ Int.* **2001**, *41*, 1309–1315. [CrossRef]
15. Jung, I.H. Critical evaluation and thermodynamic modeling of the Mn-Cr-O system for the oxidation of SOFC interconnect. *Solid State Ionics* **2006**, *177*, 765–777. [CrossRef]
16. Lins, V.D.F.C.; Madeira, L.; Vilela, J.M.C.; Andrade, M.S.; Buono, V.T.L.; Guimarães, J.P.; Alvarenga, E.D.A. Selective oxidation of dual phase steel after annealing at different dew points. *Appl. Surf. Sci.* **2011**, *257*, 5871–5878. [CrossRef]
17. Wang, H.; Jin, X.; Hu, G.; He, Y. Changing oxide layer structures with respect to the dew point prior to hot-dip galvanizing of  $\delta$ -TRIP steel. *Surf. Coat. Technol.* **2018**, *337*, 260–269. [CrossRef]
18. Yang, Q.; Luo, J.L. Effects of Hydrogen on Disorder of Passive Films and Pitting Susceptibility of Type 310 Stainless Steel. *J. Electrochem. Soc.* **2001**, *148*, B29. [CrossRef]
19. Guo, L.Q.; Qin, S.X.; Yang, B.J.; Liang, D.; Qiao, L.J. Effect of hydrogen on semiconductive properties of passive film on ferrite and austenite phases in a duplex stainless steel. *Sci. Rep.* **2017**, *7*, 8–13. [CrossRef]
20. Bao, B.; Liu, J.; Xu, H.; Liu, B.; Zhang, K.; Jin, Z. Insight into a high temperature selective oxidation of HP40 alloy under a H<sub>2</sub>-H<sub>2</sub>O environment. *RSC Adv.* **2017**, *7*, 8589–8597. [CrossRef]
21. Pardo Sainz, M.; Campo Ruiz, J.J. ¿Podría Estabilizarse una Fase Helicoidal en Mn<sub>1-x</sub>Mg<sub>x</sub>Cr<sub>2</sub>O<sub>4</sub>? Master's Thesis, Universidad de Zaragoza, Zaragoza, Spain, 2019.
22. Dutta, B.; Pal, D. Absorption and Raman spectroscopy: Ferrimagnet spinel MnCr<sub>2</sub>O<sub>4</sub>. *AIP Conf. Proc.* **2019**, *2115*, 2–6.
23. Kjellqvist, L. Thermodynamic Description of the Fe-C-Cr-Mn-Ni-O System. Ph.D. Thesis, KTH Industrial Engineering and Management, Stockholm, Sweden, 2009.
24. Greenwood, N.N.; Earnshaw, A. (Eds.) Manganese, Technetium and Rhenium. In *Chemistry of the Elements*, 2nd ed.; Butterworth-Heinemann: Oxford, UK, 1997; pp. 1040–1069, ISBN 978-0-7506-3365-9.
25. Biesinger, M.C.; Payne, B.P.; Grosvenor, A.P.; Lau, L.W.M.; Gerson, A.R.; Smart, R.S.C. Resolving surface chemical states in XPS analysis of first row transition metals, oxides and hydroxides: Cr, Mn, Fe, Co and Ni. *Appl. Surf. Sci.* **2011**, *257*, 2717–2730. [CrossRef]
26. Curia, M.V. Estudio Físicoquímico y Catalítico Del Sistema Mn-O-V. Ph.D. Thesis, Universidad Nacional de La Plata, Buenos Aires, Argentina, 2010; p. 209. [CrossRef]
27. Hu, L.; Wang, W.; Tu, J.; Hou, J.; Zhu, H.; Jiao, S. Self-assembled amorphous manganese oxide/hydroxide spheres via multi-phase electrochemical interactions in reverse micelle electrolytes and their capacitive behavior. *J. Mater. Chem. A* **2013**, *1*, 5136–5141. [CrossRef]
28. Li, L.; Sui, J.; Qin, W. Superior capacity, rate, long cycle life and high temperature performance of multilayered porous ultralong LiMn<sub>2</sub>O<sub>4</sub> nanorods for lithium ion batteries. *J. Electroanal. Chem.* **2019**, *833*, 304–312. [CrossRef]
29. Thermo Scientific. XPS Simplified, (n.d.). Available online: <https://xpssimplified.com/index.php> (accessed on 8 September 2020).
30. Badin, V.; Diamanti, E.; Forêt, P.; Darque-Ceretti, E. Water Vapor Oxidation of Ferritic 441 and Austenitic 316L Stainless Steels at 1100 °C for Short Duration. *Procedia Mater. Sci.* **2015**, *9*, 48–53. [CrossRef]
31. Essuman, E.; Meier, G.H.; Żurek, J.; Hänsel, M.; Quadackers, W.J. The effect of water vapor on selective oxidation of Fe-Cr alloys. *Oxid. Met.* **2008**, *69*, 143–162. [CrossRef]
32. Hilson, G.; Hallam, K.R.; Flewit, P.E.J. The measurement of stresses within oxides produced on austenitic and ferritic steels using Raman spectroscopy. *Mater. Sci. Forum* **2006**, *524–525*, 957–962. [CrossRef]
33. Gao, T.; Fjellvåg, H.; Norby, P. A comparison study on Raman scattering properties of  $\alpha$ - and  $\beta$ -MnO<sub>2</sub>. *Anal. Chim. Acta* **2009**, *648*, 235–239. [CrossRef]
34. Pettersson, R.; Enecker, J.; Liu, L. Role of nickel in the oxidation of Fe-Cr-Ni alloys in air-water vapour atmospheres. *Mater. High Temp.* **2005**, *22*, 269–281. [CrossRef]
35. Asteman, H.; Svensson, J.E.; Norell, M.; Johansson, L.G. Influence of water vapor and flow rate on the high-temperature oxidation of 304L; effect of chromium oxide hydroxide evaporation. *Oxid. Met.* **2000**, *54*, 11–26. [CrossRef]
36. Othman, N.K.; Othman, N.; Zhang, J.; Young, D.J. Effects of water vapour on isothermal oxidation of chromia-forming alloys in Ar/O<sub>2</sub> and Ar/H<sub>2</sub> atmospheres. *Corros. Sci.* **2009**, *51*, 3039–3049. [CrossRef]
37. Ma, X.; Nie, X.; Zhao, J.; Shrotriya, P.; Zhang, Y.; Cui, Y.; Wang, J. Effect of nanosecond pulsed laser parameters on the color making of 304 stainless steel. *Opt. Laser Technol.* **2020**, *126*, 106104. [CrossRef]